Chemical trends of substitutional transition-metal dopants in diamond: An *ab initio* study

T. Chanier, C. Pryor, and M. E. Flatté

Optical Science and Technology Center and Department of Physics and Astronomy, University of Iowa, Iowa City, Iowa 52242, USA

The electronic and magnetic properties of neutral substitutional transition-metal dopants in diamond are calculated within density-functional theory using the generalized gradient approximation to the exchange-correlation potential. Ti and Fe are nonmagnetic, whereas the ground states of V, Cr, and Mn are magnetic with a spin entirely localized on the magnetic ion. For Co, Ni, and Cu, the ground state is magnetic with the spin distributed over the transition-metal ion and the nearest-neighbor carbon atoms; furthermore a bound state is found in the gap that originates from the hybridization of the $3d$-derived level of the dopant and the $2p$-derived dangling bonds of the nearest-neighbor carbons. A p-d hybridization model is developed in order to describe the origin of the magnetic interaction. This model predicts high-spin to low-spin transitions for Ni and Cu under compressive strain.

I. INTRODUCTION

Diamond has attracted great interest recently for quantum information science because of its wide band gap and the existence of more than 500 optically addressable centers,[1] many with long spin coherence times. An extensively studied color center is the nitrogen vacancy (NV) center, consisting of a carbon vacancy with a nearest-neighbor (NN) substitutional nitrogen atom. In its negatively charged state, the NV$^-$ center carries a spin $S = 1$, which is split by the C_{3v} symmetry environment of the spin center;[2] its spin state has been proposed as a qubit for quantum computation. Spin initialization and readout have been demonstrated by optical pumping and absorption measurements[3] at the zero phonon line (ZPL) at 1.945 eV. Spin manipulation has been achieved by microwave manipulation[4–6] and also through the interaction of the NV$^-$ center spin with a nitrogen nuclear spin[4] or another nearby substitutional nitrogen electron spin.[7] However, the NV$^-$ center has a large phonon sideband at room temperature that may limit its use for quantum information processing.[8]

Other applications, like quantum optics and quantum cryptography, require stable, bright, and narrow linewidth single-photon sources (SPSs). Potential optical centers for SPSs in diamond are the NV$^-$ center, the silicon-vacancy (SiV) center,[9,10] Ni-related centers,[9,11–14] and Cr-related centers.[15,16] The large phonon sideband of the NV$^-$ center spreads the emission over 100 nm in wavelength, resulting in a Debye-Waller factor of less than 5%, which is not ideal for quantum key distribution.[8] The SiV center, formed by a substitutional Si next to a vacancy, has been proposed as a stable SPS with a ZPL at 738 nm, but its fast nonradiative decay degrades its fluorescence[10] and ultimately its reliability.

Transition-metal (TM) dopants have also been studied in diamond, however initial studies focused on TM impurities in natural diamond, or in some synthetic diamond, due to the use of the TM as a solvent catalyst during the high-pressure high-temperature growth process.[17–20] Among the Ni-related centers, the NE8 center, formed by a substitutional Ni with four NN nitrogen atoms, is responsible for a ZPL at 793 nm with a narrow phonon sideband, but its low reproducibility impedes its use for applications. Among Cr-related centers, a ZPL at 749 nm[15] has been attributed to an interstitial chromium and

two other ZPLs at 744 and 764 nm have been detected but the source has not yet been identified.[16] TM dopants can also be introduced by ion implantation[14,15] or during chemical vapor deposition.[13,16] An ion-implantation approach,[14,15] and also the possibility for local-probe-mediated methods of single-ion implantation,[21,22] offer the possibility of introducing the dopants substitutionally, without additional atoms or as part of a defect complex, and also controlling the charge state through local electric fields.[22,23] Co- and Ni-related centers, with different nitrogen, boron, and vacancy complexes, have been studied in various charge states by generalized gradient approximation (GGA) calculations,[24,25] finding neutral substitutional Co to be stable in pure diamond for a Fermi energy E_F between 3.0 and 3.6 eV, and neutral substitutional Ni to be stable for E_F between 2.6 and 3.0 eV.

Transition-metal spin centers in diamond offer several potential advantages over other spin centers, including (1) the availability of states associated with the d levels of the dopant that both strongly hybridize (those of t_2 symmetry) and weakly hybridize (those of e symmetry) with the p states of the host diamond,[26,27] (2) the high symmetry of the substitutional dopant (tetrahedral group, which means the crystal field does not split angular momentum 1 triplets[28,29]), and (3) the availability of larger spin-orbit interactions through the d electrons, which may permit faster manipulation of a spin through an electric field (e.g., Refs. 28 and 29). Challenges for these spin centers include the large strain introduced when they are placed substitutionally (although formation energies have previously been found to be moderate) and the potential lower spin coherence time due to the larger spin-orbit interaction.

To clarify these phenomena we present a first-principles study of substitutional transition-metal (TM$_s$) dopants in diamond. Whereas TM$_s$ dopants may exist in several different charge states in diamond, we concentrate our study on the neutral substitutional TM dopant (TM$_s^0$) and the chemical trends within the $3d$ row of the periodic table. For each TM$_s^0$ dopant we determine the ground-state configuration, including the charge and spin state. We find for Ti through Cu a single p-d hybridization model explains the electronic and magnetic properties of the defect. Sc and Zn, which occur at the ends of the row, are not described by this model. In Sec. II, we

present a description of the method used throughout the study. In Sec. III, we present the results. We first present the chemical trends within the series from Sc to Zn and then detail the results for the most technologically interesting cases, Cr_s^0, Ni_s^0, and Cu_s^0. In the last paragraph, we describe changes under strain of the ground-state spin for Ni and Cu and contrast with Cr (which is largely unchanged by strain). In Sec. IV we comment on the implications of these results and the strain-induced spin changes for quantum information processing.

II. METHOD

The calculations were performed with the scalar relativistic version of the full potential, all-electron local-orbital FPLO 9.00-33 code.[30] In the FPLO method, a minimum basis approach with optimized local orbitals is employed, which allows for accurate and efficient total-energy calculations. The exchange and correlation potential were treated using the (spin-polarized) generalized gradient approximation [(S)GGA] with the parametrization of Perdew, Burke, and Ernzerhof.[31] The convergence of the results with respect to **k**-space integrals was carefully checked. We found that a $8 \times 8 \times 8$ **k**-point grid was sufficient to obtain convergence of the total-energy difference between spin-polarized (SGGA) and spin unpolarized (GGA) calculations.

We used a 64-atom TMC_{63} (TM = Sc, Ti, V, Cr, Mn, Fe, Co, Ni, Cu, Zn) supercell corresponding to a $2 \times 2 \times 2$ multiple of the diamond conventional cell with a TM substituted for one carbon. We fixed the supercell to correspond to the experimental lattice constant[32] of diamond $a_0 = 3.5668$ Å, and all the atomic positions within the supercell were allowed to relax with a precision of 1 meV/Å. We considered here only T_d-symmetric atomic relaxation. As a check, we did a fully-relaxed-atoms calculation without any symmetry constraints (C_1) for the NiC_{63} supercell. The C_1 relaxed calculation is about 2 meV higher in energy than the T_d relaxed calculation, which rules out such a symmetry-breaking distortion. We limited our study to high-symmetry substitutional TM impurities because these defects are among the most stable TM-related defects.[33] As charge effects have been treated elsewhere,[33] we limit our study to the neutral substitutional TM impurities and study the chemical trends within the TM series from Sc to Zn. It is to be emphasized that, in contrast to Ref. 33, we explain the chemical trends by a single p-d hybridization scheme, which provides, along with the Kohn-Sham energy-level occupation number, a clear picture of the nature of the magnetic interaction along the TM_s^0 series.

III. RESULTS

A. Transition-metal dopant ground-state spin configurations

The SGGA results are summarized in Table I. The most stable magnetic solution is obtained for Cr_s^0, with a magnetic energy $E_M = -1006$ meV, corresponding to an $S = 1$ ground state E_M lower in energy than the nonmagnetic GGA solution. Less stable magnetic solutions ($E_M \sim -250$ meV) are obtained for the $3d$ neighbors V_s^0 and Mn_s^0, which we shall see below become magnetic in a similar fashion to Cr_s^0. A different origin is found for magnetism in Co_s^0, Ni_s^0, and Cu_s^0, which have much smaller magnetic energies of ~ -100 meV. Sc_s^0 and Zn_s^0

TABLE I. TMC_{63} SGGA results: R is the NN relaxation, $E_M = E_{SGGA} - E_{GGA}$ is the magnetic energy, M_T is the total magnetization, M_{TM} (M_C) is the on-site magnetization on the TM ion (NN C atom), and N_{TM} (N_C) is the calculated number of electrons on the TM ion (NN C atom).

TM	R (%)	E_M (meV)	M_T (μ_B)	M_{TM} (μ_B)	M_C (μ_B)	N_{TM}	N_C
Sc	23.2	−49	1.0	0.2	0.2	19.3	6.4
Ti	19.0	0	0.0	0.0	0.0	20.1	6.5
V	16.7	−249	1.0	1.0	0.0	21.2	6.5
Cr	14.8	−1006	2.0	2.0	0.0	22.3	6.4
Mn	13.3	−246	1.0	1.0	0.0	23.5	6.4
Fe	12.2	0	0.0	0.0	0.0	24.6	6.4
Co	12.9	−42	1.0	0.6	0.1	25.9	6.3
Ni	14.2	−71	2.0	0.9	0.2	26.9	6.3
Cu	15.7	−127	3.0	0.8	0.4	28.1	6.2
Zn	16.6	−100	2.0	0.2	0.3	29.0	6.3

are included to complete the $3d$ row, however the magnetism of these ions differs from that of all the other $3d$ ions.

Figure 1 shows the calculated total magnetization of TMC_{63} supercells. Ti and Fe are nonmagnetic. We obtain for Cr and Ni a total magnetization $M_T = 2\,\mu_B$, corresponding to a total spin $S = 1$, although we shall see later that these two spin centers differ greatly due to the importance of different d orbitals in creating the ground-state spin. Zn, also with $S = 1$, differs from both as it has a closed d shell. For Sc, V, Mn, and Co, we obtain a total magnetization $M_T = 1\,\mu_B$, corresponding to a total spin $S = \frac{1}{2}$. The highest total magnetization is obtained for Cu with $M_T = 3\,\mu_B$ corresponding to a total spin $S = \frac{3}{2}$.

For V_s^0, Cr_s^0, and Mn_s^0, the total magnetization of $M_T = 1.0$, 2.0, and 1.0 μ_B is entirely localized on the TM ion, whereas for Co_s^0, Ni_s^0, and Cu_s^0 the total magnetization of $M_T = 1.0$, 2.0, and 3.0 μ_B is distributed between the TM ion and the NN carbon atoms with a TM ion magnetization of $M_{TM} = 0.6$, 0.9, and 0.8 μ_B and a NN carbon atom magnetization of $M_C = 0.1$, 0.2, and 0.4 μ_B, corresponding to a total magnetic moment of 0.4, 0.8, and 1.6 μ_B distributed over the NN C. The number of electrons located on the TM ion compared to its atomic number and the number of electrons on the NN carbon atoms allow us to identify the configuration of the TM ion and the induced charge on the NN carbons. From Ti to Fe, the TM
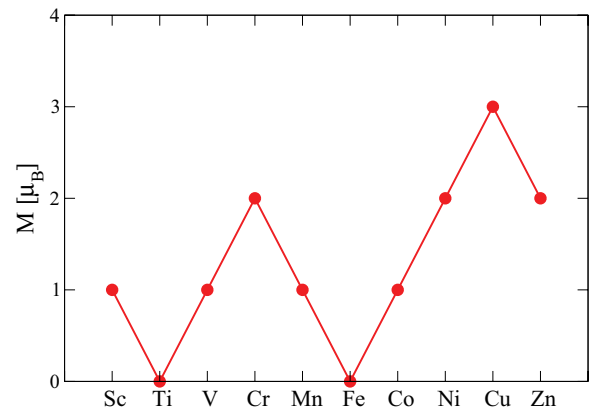

FIG. 1. (Color online) TMC_{63} SGGA total magnetic moment.

occupation number is consistent with a TM^{2+} configuration $4s^0 3d^n$ ($n = 2, 3, 4, 5, 6$) and the TM^{2+} ion induces two extra electrons distributed over the four NN carbon dangling bonds with a local charge on each NN carbon atom $Q_C \sim 0.5$. For Co, Ni, and Cu, the TM occupation number is consistent with a TM^+ configuration $4s^0 3d^{n+1}$ ($n = 7, 8, 9$) and the TM^+ ion induces one extra electron distributed over the four NN carbon dangling bonds with a local charge on each NN carbon atom $Q_C \sim 0.2$. Sc and Zn differ greatly from all the other $3d$ dopants and hence will be discussed only at the end.

When a carbon atom is removed from the ideal diamond lattice, it creates a C vacancy with four dangling-bond orbitals occupied by four electrons. The tetrahedral symmetry of the carbon vacancy implies the formation of symmetry adapted molecular orbitals of a_1 and t_2 symmetry. The SGGA a_1 level is formed primarily of NN carbon $2s$ orbitals whereas the SGGA t_2 levels are primarily formed by NN carbon $2p$ orbitals. In substitutional position, the TM ion will occupy the carbon vacancy site and will be at the center of a tetrahedron formed by the four NN carbon atoms, implying a crystal field of T_d symmetry. This T_d crystal field will split the single-particle $3d$ manifold into a doubly degenerate e level and a triply degenerate t_2 level. For tetrahedral bonding the t_2 levels are expected to be higher in energy than the e levels. The TM t_2 levels will hybridize with the NN carbon dangling bond of t_2 symmetry and form bonding (t_B) and antibonding (t_{AB}) hybrid levels. This p-d hybridization model[26,27] helps explain the origin of the magnetic interaction and differentiate the nature of the magnetic interaction along the series. Due to the high-energy position of the TM $4s$ level compared to the C_{NN} $2s$ states, its hybridization will be negligible and the a_1 level will remain of primarily C_{NN} $2s$ character. We will neglect the a_1 levels in the following discussion as they do not participate in the magnetic interaction. Table II gives the configuration of the TM ion and the NN carbon dangling bond consistent with the Kohn-Sham energy-level occupation number. For TM = V, Cr, and Mn, the magnetization is then driven by the e bound states with the magnetization entirely localized on the TM ion in the TM^{2+} configuration $4s^0 3d^n$. The two extra electrons induced by the TM^{2+} ion will occupy the dangling bonds and form a nonmagnetic C_{NN} defect level of configuration $2s^2 2p^4$. For TM = Co, Ni, and Cu, we start to occupy the antibonding t_{AB} bound states and the magnetization

TABLE II. TM ion and NN carbon dangling-bond occupation consistent with the Kohn-Sham energy-level occupation.

| TM	TM conf.	DB conf.	KS energy-level occupation
Sc	$3d^1 4s^0$	$2s^2 2p^4$	$(t_B^\uparrow)^3 (t_B^\downarrow)^2$
Ti	$3d^2 4s^0$	$2s^2 2p^4$	$(t_B^\uparrow)^3 (t_B^\downarrow)^3$
V	$3d^3 4s^0$	$2s^2 2p^4$	$(t_B^\uparrow)^3 (t_B^\downarrow)^3 (e^\uparrow)^1 (e^\downarrow)^0$
Cr	$3d^4 4s^0$	$2s^2 2p^4$	$(t_B^\uparrow)^3 (t_B^\downarrow)^3 (e^\uparrow)^2 (e^\downarrow)^0$
Mn	$3d^5 4s^0$	$2s^2 2p^4$	$(t_B^\uparrow)^3 (t_B^\downarrow)^3 (e^\uparrow)^2 (e^\downarrow)^1$
Fe	$3d^6 4s^0$	$2s^2 2p^4$	$(t_B^\uparrow)^3 (t_B^\downarrow)^3 (e^\uparrow)^2 (e^\downarrow)^2$
Co	$3d^8 4s^0$	$2s^2 2p^3$	$(t_B^\uparrow)^3 (t_B^\downarrow)^3 (e^\uparrow)^2 (e^\downarrow)^2 (t_{AB}^\uparrow)^1 (t_{AB}^\downarrow)^0$
Ni	$3d^9 4s^0$	$2s^2 2p^3$	$(t_B^\uparrow)^3 (t_B^\downarrow)^3 (e^\uparrow)^2 (e^\downarrow)^2 (t_{AB}^\uparrow)^2 (t_{AB}^\downarrow)^0$
Cu	$3d^{10} 4s^0$	$2s^2 2p^3$	$(t_B^\uparrow)^3 (t_B^\downarrow)^3 (e^\uparrow)^2 (e^\downarrow)^2 (t_{AB}^\uparrow)^3 (t_{AB}^\downarrow)^0$
Zn	$3d^{10} 4s^1$	$2s^2 2p^3$	$(t_B^\uparrow)^3 (t_B^\downarrow)^3 (e^\uparrow)^2 (e^\downarrow)^2 (t_{AB}^\uparrow)^3 (t_{AB}^\downarrow)^1$
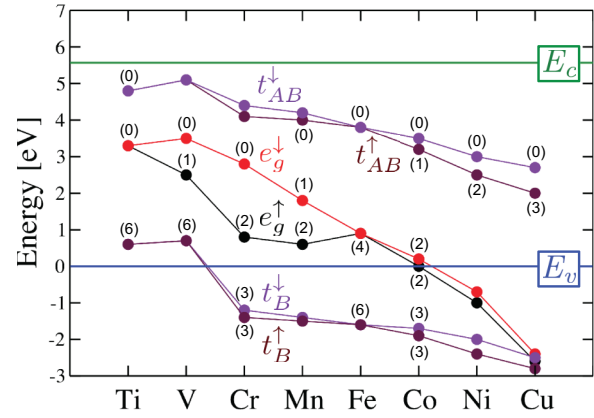
FIG. 2. (Color online) Single-particle TM $3d$-derived SGGA Kohn-Sham (KS) energy levels of TMC63 calculation. TM $3d$ levels are split by the tetrahedral crystal field into e^σ and t_2^σ levels. The bonding and antibonding levels (t_B^σ and t_{AB}^σ) are the results of the hybridization between the TM t_2 and NN carbon $2p$-derived t_2 levels. E_v (energy reference) and E_c are the SGGA valence-band maximum and (direct) conduction-band minimum of pure diamond. In parentheses are indicated the occupation number of the KS energy levels.

is delocalized on the TM ion and the C_{NN}s. The TM is in the TM^+ configuration $4s^0 3d^{n+1}$ which induces one extra electron distributed over the NN carbon atoms. This extra electron will occupy the dangling bonds and form a defect level of configuration $2s^2 2p^3$ which induces a nonzero magnetic moment on the NN carbon atoms. This situation is consistent with a local Hund exchange coupling dominating the crystal field as we will see for the high-spin (HS) configuration of Ni_s^0 and Cu_s^0 without strain. In those cases, the application of strain will give rise to a low-spin (LS) configuration, which can be explained by a competition between the local Hund exchange coupling and the crystal field.

The TM $3d$-derived Kohn-Sham states within the series from Ti to Cu are presented in Fig. 2. The GGA direct and indirect band gaps for pure diamond are, respectively, $E_{GGA}^D = E_c - E_v = 5.6$ and $E_{GGA}^{Ind} = 4.3$ eV, both of which are smaller than the experimental gap ($E_G^{Ind} = 5.47$ eV) due to the well-known gap underestimation of the GGA functional.[34] As mentioned earlier, the tetrahedral crystal field will split the single-particle $3d$ manifold into a doubly degenerate e level and a triply degenerate t_2 level. The symmetry of the bonds from the four nearest neighbors is compatible with t_2 symmetry,[26] but not with e symmetry. Thus the $3d$-derived t_2 level hybridizes with the NN carbon $2p$-derived t_2 states to form bonding t_B and antibonding t_{AB} hybrid states. Due to the strong hybridization between the TM ion and the NN carbon atoms, the $3d$-derived hybrid states will form bound states in the gap.[27,35,36]

For the nonmagnetic Ti_s^0 impurity, there are three bound states in the gap: a totally occupied (sixfold degenerate) t_B level situated at $E_v + 0.6$ eV, a totally empty (fourfold degenerate) e level at $E_v + 3.3$ eV, and a totally empty (sixfold degenerate) t_{AB} level at $E_v + 4.8$ eV. For V_s^0, Cr_s^0, and Mn_s^0, the spin-up and spin-down (threefold degenerate) t_B levels are totally occupied and nearly spin degenerate. For V, the t_B forms a bound state at $E_v + 0.7$ eV and, for Cr_s^0 to Cu_s^0, the t_B state forms a crystal-field resonance state inside the valence

band which (with increasing atomic number) decreases in energy. For V, Cr, and Mn, the occupation difference of the spin-up and spin-down e bound states is responsible for the total magnetization localized on the TM ion; the Cr e level configuration is $(e^\uparrow)^2(e^\downarrow)^0$, corresponding to a total magnetic moment $M_T = 2.0\ \mu_B$ ($S = 1$). The absence of magnetism for Fe is due to a totally occupied spin-degenerate e level (fourfold degenerate). For the next three dopants in the series (Fig. 1), Co, Ni, and Cu, the e levels remain totally occupied and enter the valence band. For these dopants the spin-up antibonding (threefold degenerate) $t_{AB}^\uparrow$ state starts to become occupied, with one, two, or three electrons, respectively, while the spin-down antibonding $t_{AB}^\downarrow$ level remains totally empty. For Co_s^0, Ni_s^0, and Cu_s^0, the occupation difference of the spin-up and spin-down t_{AB} bound states is responsible for the total magnetization that is distributed over the TM ion and the NN carbon atoms through the hybrid t_{AB} level; for example, the Ni t_{AB} level configuration is $(t_{AB}^\uparrow)^2(t_{AB}^\downarrow)^0$, corresponding to a total magnetic moment $M_T = 2.0\ \mu_B$ ($S = 1$) distributed over the Ni ion and the NN carbon atoms.

We now discuss the outliers Sc_s^0 and Zn_s^0. Sc $3d$ levels hybridize slightly with the NN carbon t_2 levels and give rise to two spin-up and two spin-down bound states situated at 0.7 and 1.2 eV (1.0 and 1.6 eV). The spin-down t_2 level at 1.6 eV is partially empty (one hole) which is responsible for the total spin polarization $M_T = 1\ \mu_B$ which is distributed on the Sc and NN carbon atoms. The two spin-degenerated peaks at 4.6 eV arises from the Sc e levels. There are no antibonding levels and the density of states cannot be explained by the p-d hybridization model used above for Ti through Cu. Zn gives rise to two bound states of t_2 symmetry at 1.6 and 2.1 eV above the valence-band maximum (VBM) which are almost entirely of NN carbon $2p$ character. The partially empty (two holes) bound state at 2.1 eV above the VBM is responsible for the total magnetization $M_T = 2\ \mu_B$ which is distributed over the Zn and NN carbon atoms. The number of electrons on Zn is 29.0 corresponding to a configuration $3d^{10}\,4s^1$. Thus the Zn $4s$ level is almost depleted and the Zn $4s$ electron occupies a bound state of mostly NN carbon $2p$ character to lower its energy. The Zn^+ $3d$ levels are delocalized and are located at about -6 eV below the top of the valence band and are nearly spin degenerate, corresponding to a nonmagnetic $3d^{10}$ closed-shell configuration.

In the next subsections, we will present the electronic structure of the most interesting TM_s^0 dopants for potential application, namely, the $S = 1$ dopants Cr_s^0 and Ni_s^0 and the $S = \frac{3}{2}$ dopant Cu_s^0. Those dopants will have dramatically different origins for the magnetism, depending on whether the magnetism is driven by the e states or the t_{AB} states. This difference will also lead to a very different response of the ground-state spin to strain, as treated in the last paragraph. For those transition metal dopants discussed here, but not further in Sec. III, figures showing the spin-resolved density of states and level diagrams for the schematic p-d hybridization model, similar to Fig. 3, are shown in the Supplemental Material.[37]

B. The $S = 1$ centers: Cr_s^0 and Ni_s^0.

Figure 3 shows the total, Cr, and NN carbon partial SGGA density of states (DOS) of the CrC_{63} supercell. The Cr $3d$
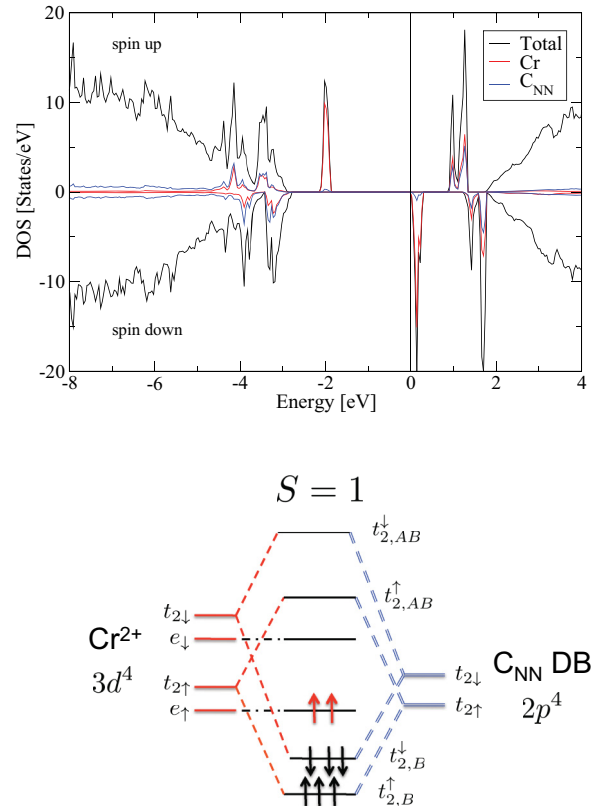

FIG. 3. (Color online) Top: total, Cr, and NN C partial DOS. For these and subsequent such plots the upper portion of the plot is for the majority spin and the lower portion is for the minority spin; here the partial DOSs are the same as the ion is nonmagnetic. The bonding state t_B is delocalized across the Ti $3d$ and NN C $2p$ states. Bottom: schematic representation of the p-d hybridization model for Cr_s^0.

levels are split by the T_d crystal field into e and t_2 levels. Cr t_2 levels hybridize with the NN carbon $2p$ levels to form bonding t_B and antibonding t_{AB} hybrid levels. The bonding t_B levels are nearly spin degenerate and form crystal-field resonance states around -1.5 eV below the VBM. The spin-up and spin-down e levels are localized on the Cr site, giving rise to two bound states approximately 0.8 and 2.8 eV above the VBM and separated by a Hund exchange splitting $J^H = 2$ eV. The Cr e level contribution to the total magnetization is roughly 80% of the total magnetization and the bonding t_B states are weakly spin polarized. The antibonding t_{AB} levels are totally empty and form two bound states around 4.3 eV above the VBM. The number of electrons located on the Cr ion is 22.3, which corresponds to a Cr^{2+} configuration $4s^0\,3d^4$ and spin $S_1 = 1$. Cr^{2+} induces two extra electrons distributed over NN carbon dangling bonds of configuration $2s^2\,2p^4$ and spin $S_2 = 0$. The Cr $(t_2)^2$ level hybridizes with the NN carbon $2p^4$ t_2 defect level. The bonding t_B states are fully occupied and the e levels are partially occupied in the configuration $(e^\uparrow)^2(e^\downarrow)^0$ corresponding to a total magnetic moment $M_T = 2.0\ \mu_B$ entirely localized on the Cr ion. Figure 3 explains the observed DOS by a p-d hybridization model.

Figure 4 shows the total, Ni, and NN carbon partial SGGA density of states (DOS) of the NiC_{63} supercell. The Ni $3d$ levels are split by the T_d crystal field into e and t_2 levels. Ni t_2 levels
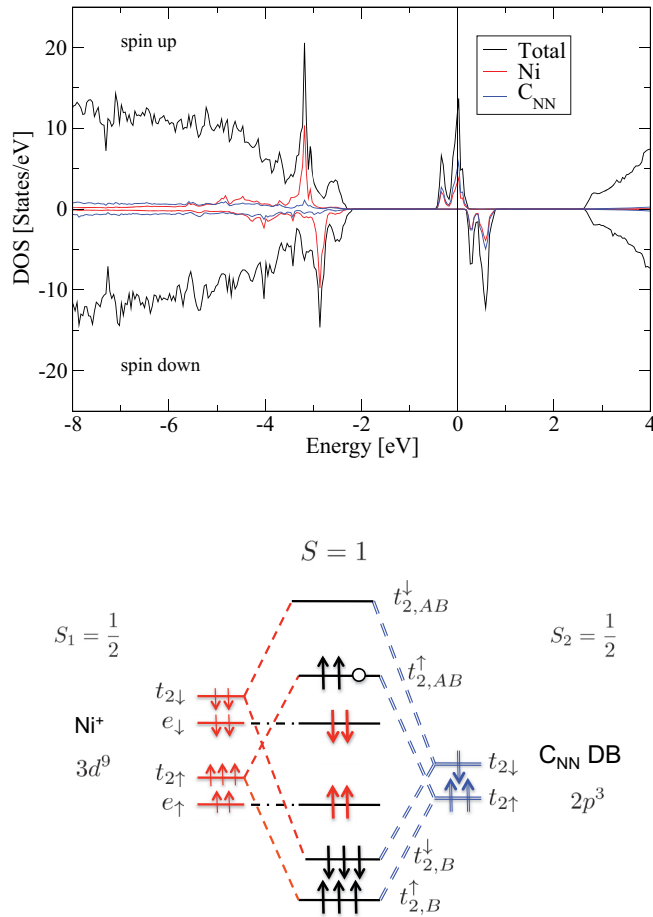
FIG. 4. (Color online) Top: total, Ni, and NN C partial DOS. Bottom: schematic representation of the p-d hybridization model for Ni_s^0.

FIG. 5. (Color online) Top: total, Cu, and NN C partial DOS. Bottom: schematic representation of the p-d hybridization model for Cu_s^0. Symbols are the same as in Fig. 3.

hybridize with the NN carbon $2p$ levels to form bonding t_B and antibonding t_{AB} hybrid levels. The spin-up and spin-down bonding t_B levels forms a crystal-field resonance state situated around -2.1 eV below the VBM. The spin-up and spin-down e levels are localized on the Ni site, giving rise to two peaks approximately 1 eV below the valence-band maximum (VBM) and separated by a Hund exchange splitting $J^H = 0.4$ eV. The spin-up and spin-down antibonding t_{AB} levels are located at 2.5 and 3.0 eV above the VBM. The antibonding t_{AB} level contribution to the total magnetization is more than 70%, with 50% from the Ni $3d$ level and 20% from the NN carbon $2p$ level. The number of electrons located on the Ni ion is 26.9, which corresponds to a Ni^+ configuration $4s^0 3d^9$ with a spin $S_1 = \frac{1}{2}$. Ni^+ induces one extra electron distributed over the four NN carbon dangling bonds of configuration $2s^2 2p^3$ and spin $S_2 = \frac{1}{2}$. The Ni t_2 levels hybridize with the NN carbon $2p^3 t_2$ defect level. This p-d hybridization picture identifies the origin of the calculated SGGA DOS as due to a FM interaction between S_1 and S_2 as shown in Fig. 4.

C. The $S = \frac{3}{2}$ center: Cu_s^0.

Figure 5 shows the total, Cu, and NN carbon partial DOS of the CuC_{63} supercell. The Cu $3d$ levels are split by the T_d crystal field into e and t_2 levels. Cu t_2 levels hybridize with the
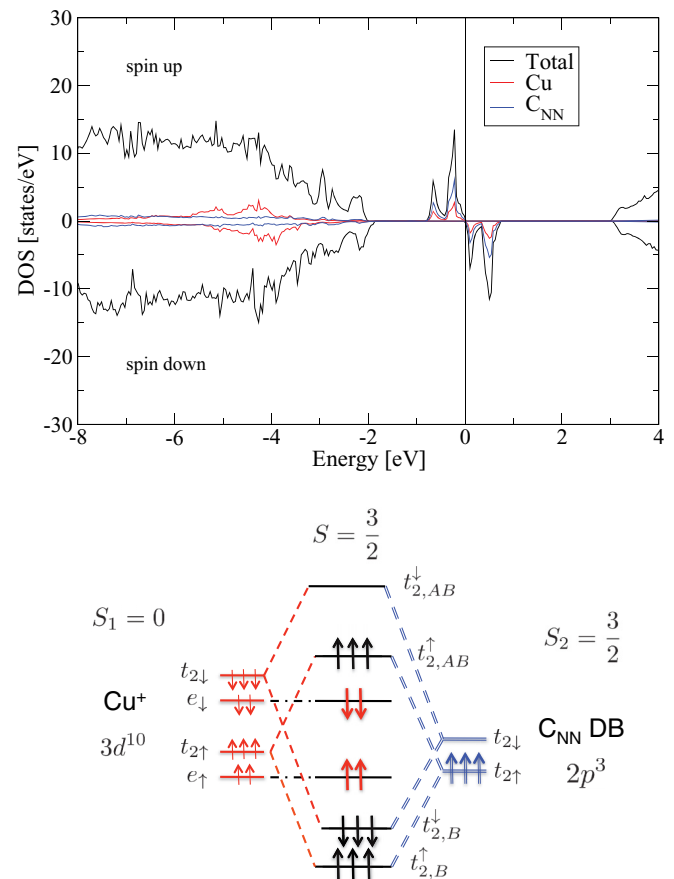
NN carbon $2p$ levels to form bonding t_B and antibonding t_{AB} hybrid levels. The bonding t_B levels are weakly spin polarized and are located around 2.6 eV below the VBM. The spin-up and spin-down e levels are localized on the Cu site, giving rise to two nearly spin-degenerate peaks situated around 2.4 eV below the VBM. The spin-up and spin-down antibonding t_{AB} levels are situated at 1.9 and 2.7 eV above the VBM. The number of electrons located on the Cu ion is 28.1, which corresponds to a Cu^+ configuration $4s^0 3d^{10}$ and a spin $S_1 = 0$. Cu^+ induces one extra electron distributed over the NN carbon dangling bonds of configuration $2s^2 2p^3$ and spin $S_2 = \frac{3}{2}$. The Cu t_2 level hybridizes with the NN carbon $2p^3 t_2$ defect level. The $2p^3$ configuration of the NN carbon dangling bond is responsible for the total spin $S = \frac{3}{2}$ ($M_T = 3.0$ μ_B), which is distributed over the Cu ($M_{Cu} = 0.8$ μ_B) and the four NN carbon atoms ($M_C = 0.4$ μ_B). Figure 5 explains the observed DOS by a p-d hybridization model. Cu^+ $3d$ levels are nearly spin degenerate, corresponding to a nonmagnetic $3d^{10}$ closed-shell configuration.

D. High-spin to low-spin transition with strain

We now study the effect of hydrostatic pressure on the magnetic properties of high-spin TM_s^0 dopants (TM = Cr, Ni, and Cu). For that purpose, we take the total-energy difference between high-spin (HS) and low-spin (LS) fixed spin
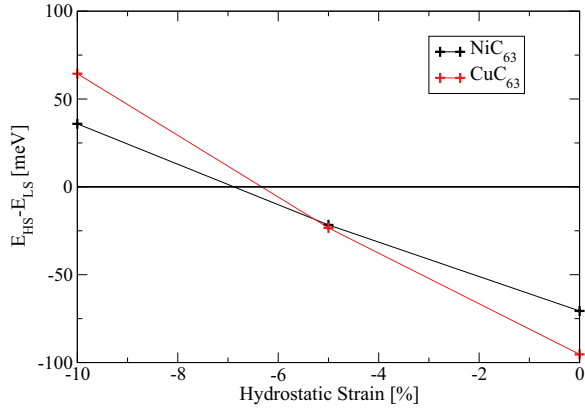
FIG. 6. (Color online) Total-energy difference between low-spin and high-spin fixed spin moment SGGA calculations as a function of hydrostatic strain.

calculations. The HS (LS) state of Cr_s^0 and Ni_s^0 corresponds to a total magnetic moment $M_{HS} = 2\ \mu_B$ ($M_{LS} = 0\ \mu_B$) whereas the HS (LS) state of Cu_s^0 corresponds to $M_{HS} = 3\ \mu_B$ ($M_{LS} = 1\ \mu_B$). For Cr_s^0, we do not obtain a transition due to the large magnetic energy of the $S = 1$ ground state, about 1 eV energetically lower than the $S = 0$ nonmagnetic solution. The energetic stability of the magnetic ground state is associated with the e character of the highly spin-polarized states, whereas both Ni and Cu have magnetism driven by the t_2 states. The results for Ni_s^0 and Cu_s^0 are presented in Fig. 6. We obtain a transition from high-spin $S = 1$ ($S = \frac{3}{2}$) to low-spin $S = 0$

$(S = \frac{1}{2})$ under compressive hydrostatic strain with a transition at $e_H = -7\%$ ($e_H = -6\%$) for Ni_s^0 (Cu_s^0).

Figures 7 and 8 present the DOS of the low-spin SGGA ground state of Ni_s^0 and Cu_s^0 under compressive hydrostatic strain $e_H = -10\%$, corresponding to a pressure of the order of 100 GPa, which is well within the range of accessible pressures from a diamond-anvil cell.[38] The corresponding total magnetic moment for the (spin unfixed) SGGA solution is $M_{LS} = 0.1\ \mu_B$ for Ni_s^0 and $M_{LS} = 1.4\ \mu_B$ for Cu_s^0. The TM$^+$ configuration $4s^0\,3d^{n+1}$ remains unchanged, which induces an extra electron on the NN carbon atoms, creating a $2s^2 2p^3$ defect level. Figures 7 and 8 explain the observed DOS with a p-d hybridization model. For Ni_s^0, the spin-degenerate Ni $3d$ levels hybridize with the spin-degenerate $2p^3$ dangling bonds, giving rise to a nonmagnetic interaction, corresponding to an antiferromagnetic interaction between the Ni $S_1 = \frac{1}{2}$ and a spin $S_2 = -\frac{1}{2}$ distributed over the NN carbon dangling bonds. For Cu_s^0, the spin-degenerate Cu $3d$ levels hybridize with the $2p^3$ dangling bond. The $2p^3$ configuration is responsible for the total spin $S = \frac{1}{2}$ distributed over the NN carbon dangling bonds.

The nearly degenerate $S = 1$ and 0 states of the substitutional nickel impurity in diamond can be understood as an exchange-coupled system of two electron spins: one localized on the nickel ion and one delocalized on the four nearest-neighbor (NN) carbon atoms.[39] Strain changes the exchange coupling and as a result modifies the ground state from parallel to antiparallel alignment. A similar phenomenon occurs for Cu, but the transition is between $S = 3/2$ and $1/2$. The
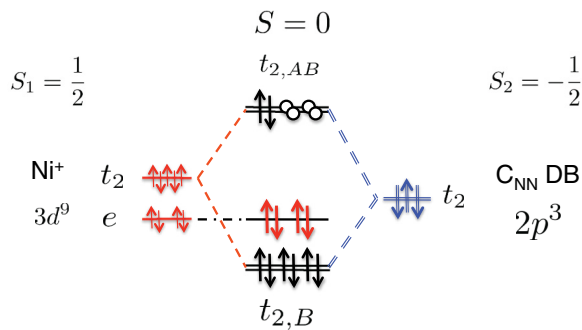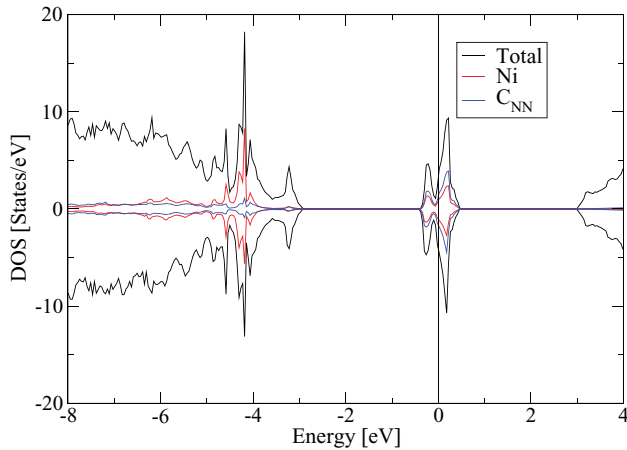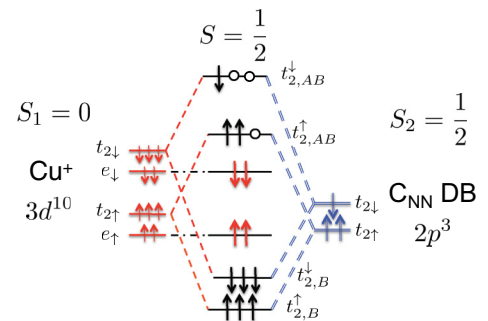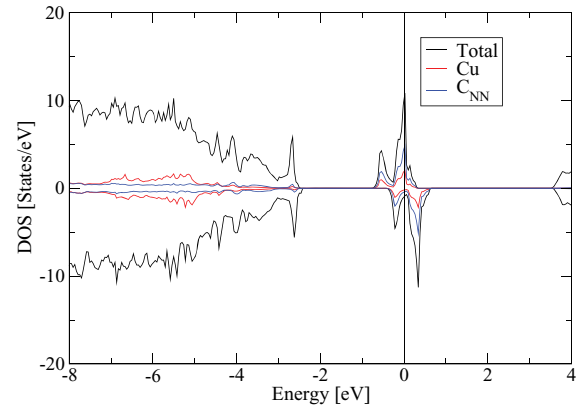

FIG. 7. (Color online) Top: total, Ni, and NN C partial DOS. Bottom: schematic representation of the p-d hybridization model for Ni_s^0. Symbols are the same as in Fig. 3.

FIG. 8. (Color online) Top: total, Cu, and NN C partial DOS. Bottom: schematic representation of the p-d hybridization model for Cu_s^0. Symbols are the same as in Fig. 3.

existence of a pressure induced transition between a high-spin and low-spin state is also observed in transition-metal-ion compounds, where it was shown theoretically to be due to a competition between localization (induced by the Hund's exchange coupling, which favors the high-spin state) and a tendency toward delocalization induced by the crystal field (which favors the low-spin state).[40]

IV. CONCLUSION

We have studied by first-principles calculations the chemical trends of neutral substitutional transition-metal dopants in diamond. The origin of the magnetism for these dopants has been explained by a p-d hybridization model. Ti and Fe impurities are nonmagnetic, corresponding to closed bonding hybridized t_2 and an empty (Ti) or full (Fe) e level, respectively. For V, Cr, and Mn, the magnetization is entirely localized on the TM ion and driven by the e levels. For Co, Ni, and Cu, the magnetization is distributed over the TM ion and the NN carbon atoms with a magnetization due to the antibonding t_2 levels. Electron paramagnetic resonance study of these magnetic centers would be of great interest in order to confirm the calculated chemical trend.

The calculated total magnetic moments for the TM ion series are in agreement with previous GGA calculations.[41] Reference 41 finds the same relaxation with point-group T_d symmetry for Ti, Cr, and Fe. They found a NN relaxation of D_{2d} for V, Mn, and Co and a C_1 symmetry relaxation for Ni. To verify the validity of our results, which were all-atom relaxation calculations performed with T_d symmetry, we did nearest-neighbor atom relaxation calculations within GGA

(1-meV/Å precision) with no symmetry constraints, fixing the other atomic positions to their ideal value. For Ni, the tetrahedra calculated this way are slightly distorted to C_1 symmetry, however the distortion is less than a 1% difference in distance and less than a 0.1% difference in angle, with a magnetic energy $E_M = 48$ meV and a total spin $S = 1$. Hence our T_d-symmetry results represent well the state of these transition-metal ions.

The nearly degenerate $S = 1$ and 0 states of the substitutional nickel impurity in diamond can be understood as an exchange-coupled system of two electron spins: one localized on the nickel ion and one delocalized on the four nearest-neighbor (NN) carbon atoms. Such nearly degenerate $S = 1$ and 0 states can be used to construct an effective two-state decoherence free subspace from the $S_z = 0$ triplet (T_0) and the singlet (S) states. This approach would be similar to that implemented for double quantum dots[42] with electrostatic gating. For the nickel ion, strain modulation could be used to manipulate the energy splitting between the S and the T_0 states, instead of the electrostatic gating used for double quantum dots.[42] This is one way that the electronic configurations of transition-metal dopants could be used to encode quantum information in a form amenable for solid-state quantum information processing.

[1] A. M. Zaitsev, *Optical Properties of Diamond: A Data Handbook* (Springer, New York, 2001).

[2] A. Lenef and S. C. Rand, Phys. Rev. B **53**, 13441 (1996).

[3] G. Davies and M. F. Hamer, Proc. R. Soc. London A **348**, 285 (1976).

[4] F. Jelezko, T. Gaebel, I. Popa, M. Domhan, A. Gruber, and J. Wrachtrup, Phys. Rev. Lett. **93**, 130501 (2004).

[5] R. Hanson, O. Gywat, and D. D. Awschalom, Phys. Rev. B **74**, 161203(R) (2006).

[6] R. Hanson, L. P. Kouwenhoven, J. R. Petta, S. Tarucha, and L. M. K. Vandersypen, Rev. Mod. Phys. **79**, 1217 (2007).

[7] R. Hanson, F. M. Mendoza, R. J. Epstein, and D. D. Awschalom, Phys. Rev. Lett. **97**, 087601 (2006).

[8] F. Jelezko, I. Popa, A. Gruber, C. Tietz, J. Wrachtrup, A. Nizovtsev, and S. Kilin, Appl. Phys. Lett. **81**, 2160 (2002).

[9] C.-H. Su, A. D. Greentree, and L. C. L. Hollenberg, Phys. Rev. A **80**, 052308 (2009).

[10] T. Feng and B. D. Schwartz, J. Appl. Phys. **73**, 1415 (1993).

[11] J. Isoya, H. Kanda, and Y. Uchida, Phys. Rev. B **42**, 9843 (1990).

[12] J. Isoya, H. Kanda, J. R. Norris, J. Tang, and M. K. Bowman, Phys. Rev. B **41**, 3905 (1990).

[13] J. R. Rabeau, Y. L. Chin, S. Prawer, F. Jelezko, T. Gaebel, and J. Wrachtrup, Appl. Phys. Lett. **86**, 131926 (2005).

[14] J. O. Orwa, I. Aharonovich, F. Jelezko, G. Balasubramanian, P. Balog, M. Markham, D. J. Twitchen, A. D. Greentree, and S. Prawer, J. Appl. Phys. **107**, 093512 (2010).

[15] I. Aharonovich, S. Castelletto, B. C. Johnson, J. C. McCallum, D. A. Simpson, A. D. Greentree, and S. Prawer, Phys. Rev. B **81**, 121201 (2010).

[16] I. Aharonovich, S. Castelletto, D. A. Simpson, A. D. Greentree, and S. Prawer, Phys. Rev. A **81**, 043813 (2010).

[17] M. Iizuka, H. Ikawa, and O. Fukunaga, Diam. Relat. Mater. **5**, 38 (1996).

[18] I. Kiflawi, H. Kanda, and S. Lawson, Diam. Relat. Mater. **11**, 204 (2002).

[19] W. Liu, H. Ma, X. Li, Z. Liang, R. Li, and X. Jia, Diam. Relat. Mater. **16**, 1486 (2007).

[20] I.-C. Lin, C.-J. Lin, and W.-H. Tuan, Diam. Relat. Mater. **20**, 42 (2011).

[21] D. Kitchen, A. Richardella, J.-M. Tang, M. E. Flatté, and A. Yazdani, Nature (London) **442**, 436 (2006).

[22] D. H. Lee and J. A. Gupta, Science **330**, 1807 (2010).

[23] A. M. Yakunin, A. Y. Silov, P. M. Koenraad, J. H. Wolter, W. Van Roy, J. De Boeck, J.-M. Tang, and M. E. Flatté, Phys. Rev. Lett. **92**, 216806 (2004).

[24] R. Larico, L. V. C. Assali, W. V. M. Machado, and J. F. Justo, J. Phys.: Condens. Mater **20**, 415220 (2008).

[25] R. Larico, J. F. Justo, W. V. M. Machado, and L. V. C. Assali, Phys. Rev. B **79**, 115202 (2009).

[26] H. P. Hjalmarson, P. Vogl, D. J. Wolford, and J. D. Dow, Phys. Rev. Lett. **44**, 810 (1980).

[27] P. Vogl and J. M. Baranowski, Acta. Phys. Polo. **A67**, 133 (1985).

[28] P. Y. Yu and M. Cardona, *Fundamentals of Semiconductors*, 3rd ed. (Springer-Verlag, Berlin, 2001).

[29] J.-M. Tang, J. Levy, and M. E. Flatté, Phys. Rev. Lett. **97**, 106803 (2006).

[30] K. Koepernik and H. Eschrig, Phys. Rev. B **59**, 1743 (1999).

[31] J. P. Perdew, K. Burke, and M. Ernzerhof, Phys. Rev. Lett. **77**, 3865 (1996).

[32] D. P. Riley, Nature (London) **153**, 587 (1944).

[33] L. V. C. Assali, W. V. M. Machado, and J. F. Justo, Phys. Rev. B **84**, 155205 (2011).

[34] C. Filippi, D. J. Singh, and C. J. Umrigar, Phys. Rev. B **50**, 14947 (1994).

[35] T. Chanier, F. Virot, and R. Hayn, Phys. Rev. B **79**, 205204 (2009).

[36] T. Dietl, Phys. Rev. B **77**, 085208 (2008).

[37] See Supplemental Material at http://link.aps.org/supplemental/10.1103/PhysRevB.86.085203 for spin-resolved density of states and level diagrams for other transition-metal dopants not described in the main text.

[38] R. J. Hemley and N. W. Ashcroft, Phys. Today **51**(8), 26 (1998).

[39] T. Chanier, C. Pryor, and M. E. Flatté, arXiv:1112.4436.

[40] R. A. Bari and J. Sivardière, Phys. Rev. B **5**, 4466 (1972).

[41] L. Assali, W. Machado, and J. Justo, Physica B **404**, 4515 (2009).

[42] J. R. Petta, A. C. Johnson, J. M. Taylor, E. A. Laird, A. Yacoby, M. D. Lukin, C. M. Marcus, M. P. Hanson, and A. C. Gossard, Science **309**, 2180 (2005).